Small-molecule targeted recruitment of a nuclease to cleave an oncogenic RNA in a mouse model of metastatic cancer

Matthew G. Costales[a], Haruo Aikawa[a], Yue Li[a], Jessica L. Childs-Disney[a], Daniel Abegg[a], Dominic G. Hoch[a], Sai Pradeep Velagapudi[a], Yoshio Nakai[a], Tanya Khan[a], Kye Won Wang[b], Ilyas Yildirim[b], Alexander Adibekian[a], Eric T. Wang[c], and Matthew D. Disney[a,1]

[a]Department of Chemistry, The Scripps Research Institute, Jupiter, FL 33458; [b]Department of Chemistry and Biochemistry, Florida Atlantic University, Jupiter, FL 33458; and [c]Department of Molecular Genetics & Microbiology, University of Florida, Gainesville, FL 32610

As the area of small molecules interacting with RNA advances, general routes to provide bioactive compounds are needed as ligands can bind RNA avidly to sites that will not affect function. Small-molecule targeted RNA degradation will thus provide a general route to affect RNA biology. A non–oligonucleotide-containing compound was designed from sequence to target the precursor to oncogenic microRNA-21 (pre–miR-21) for enzymatic destruction with selectivity that can exceed that for protein-targeted medicines. The compound specifically binds the target and contains a heterocycle that recruits and activates a ribonuclease to pre–miR-21 to substoichiometrically effect its cleavage and subsequently impede metastasis of breast cancer to lung in a mouse model. Transcriptomic and proteomic analyses demonstrate that the compound is potent and selective, specifically modulating oncogenic pathways. Thus, small molecules can be designed from sequence to have all of the functional repertoire of oligonucleotides, including inducing enzymatic degradation, and to selectively and potently modulate RNA function in vivo.

nucleic acids | RNA | chemical biology | metastatic | cancer

RNA structures are key players in important biological processes and in diseased states. The only general way to target RNA, however, is by using oligonucleotide-based approaches that preferentially target unstructured regions (1). Because RNA biology is often mediated by the structure that it forms (2), approaches to target structured RNAs are advantageous. Small molecules interacting with an RNA's 3D structure could allow specificity in activity.

One class of structured RNAs that play roles in human disease biology is noncoding microRNAs (miRs) (3). They are produced from highly structured precursors processed in the nucleus (pri-miRs) and cytoplasm (pre-miRs) by the nucleases Drosha and Dicer, respectively (Fig. 1A). An important example is miR-21 as its expression in solid tumors negatively correlates with survival in triple-negative breast cancer (TNBC) patients (Fig. 1A) (4). Herein, we describe a general strategy to endow small molecules to achieve targeted degradation of RNA transcripts through ribonuclease recruitment. These studies demonstrate that sequence-based design can afford small molecules that can target structured RNAs for enzymatic cleavage, a feature previously only known to oligonucleotides.

Results and Discussion

A sequence-based design approach termed Inforna (Fig. 1B) was used to design small molecules that target the 3D folds in pre–miR-21. Inforna uses the output of folded RNA structures that bind small molecules as determined from a library-versus-library selection (5). This analysis identified a fragment (1, Fig. 2) that bound the miR-21 Dicer site selectively with a K_d of 20 μM and inhibited in vitro Dicer processing (*SI Appendix*, Figs. S1 and S2). Treatment of TNBC cells (MDA-MB-231) with 1 (10 μM) inhibited

miR-21 production by 50%, while the levels of pre–miR-21 were increased by 1.3-fold, as expected for a compound that acts by inhibiting Dicer processing (*SI Appendix*, Fig. S3). Full miR profiling showed that 1 was modestly selective (Fig. 1D).

To optimize 1 for avidity, the RNA folds in all miR precursors in the human transcriptome were compared to pre–miR-21 (*SI Appendix*, Figs. S4–S6). Several miR precursors display the A bulge motif (5′ GAC/3′ C_G; $n = 20$), yet no other targets contained it and the adjacent U bulge (5′ UUG/3′ A_C) (*SI Appendix*, Figs. S4 and S5). Fortuitously, fragment 1 bound to both sites and assembly of two fragments of 1 to target them in a single compound afforded 2 (Figs. 1C and 2 and *SI Appendix*, Fig. S3), which selectively bound pre–miR-21 with a 20-fold enhancement over 1 (*SI Appendix*, Fig. S1).

Target engagement of 2 to pre–miR-21 in vitro and in MDA-MB-231 cells was confirmed by using Chemical Cross-Linking and Isolation by Pulldown (Chem-CLIP), a strategy that utilizes a proximity-based reaction to cross-link compounds to their cellular targets (6). Cells were treated with the active Chem-CLIP probe or an inactive control probe lacking RNA binding modules (*SI*

> ### Significance
>
> The human genome produces RNAs that do not code for protein but play important roles in biology, including causing disease. These RNAs are potential drug targets. Estimates suggest that there are 100-fold more potential RNA than protein drug targets. Despite this potential, small-molecule targeting of human RNA is rare as it is technically challenging. Here we describe a general and fast strategy to design small molecules from sequence to bind an RNA and subsequently cause its destruction. The approach was proven to destroy a cancer-causing RNA in a mouse model thereby inhibiting metastasis. Armed with these approaches, we can more deeply evaluate the potential of small-molecule therapeutics targeting RNAs.
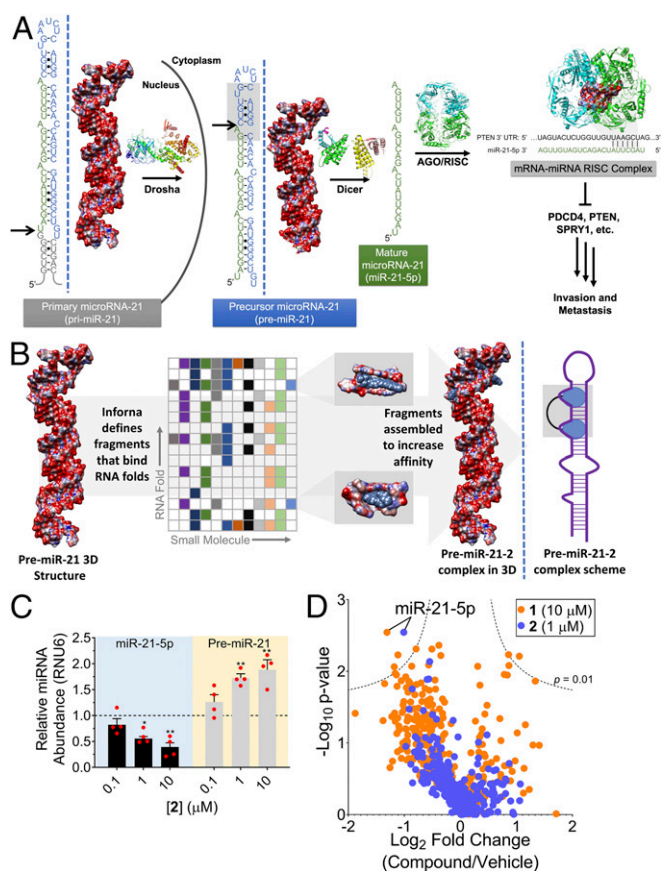
Fig. 1. Rational design of small molecules targeting microRNA-21 (miR-21). (*A*) Scheme of the processing of miR-21 hairpin precursors and its oncogenic function. Arrows indicate sites of nuclease cleavage. (*B*) The sequence-based design of monomeric (**1**) and dimeric (**2**) compounds targeting the pre–miR-21 3D structure via Inforna. (*C*) Compound **2** (Fig. 2) decreased miR-21 and increased pre–miR-21 levels in MDA-MB-231 cells. Data represent mean ± SEM ($n \geq 3$). *$P < 0.05$; **$P < 0.01$ as determined by a two-tailed Student t test. (*D*) miRNA profiling of MDA-MB-231 cells treated with **1** or **2**. Dotted lines represent a false discovery rate of 1% and variance of $S_0(0.1)$.

Appendix, Fig. S7). The active compound selectively enriched levels of pre–miR-21 by ~2.5-fold at 10 μM (*SI Appendix*, Fig. S7). Subsequently, Competitive Chem-CLIP was used to assess the relative occupancy of pre–miR-21 by **1** and **2** in MDA-MB-231 cells. Compound **2** occupied pre–miR-21 in cells 20-fold more than **1**, the predicted difference based on the affinity of the two compounds, indicating they have similar cellular permeability (*SI Appendix*, Fig. S7). The cellular binding sites of **2** within pre–miR-21 were mapped by conjugating **2** to a bleomycin RNA cleaving module and showed that, as expected, the cleavage site is proximal to the designed binding site (*SI Appendix*, Figs. S8–S10).

Compound **2** reduced miR-21 levels in cells with an IC_{50} of 1 μM. An increase in the levels of pre–miR-21 supported inhibition of biogenesis as a mode of action (Fig. 1*C*). Full miR profiling showed that **2** only significantly affected miR-21, as expected based on the design strategy (Fig. 1*D*). Proteins that are translationally repressed by miR-21 include programmed cell death protein 4 (PDCD4) and phosphatase and tensin homolog (PTEN) (7–9). Treatment of MDA-MB-231 cells with **2** increased the levels of PDCD4 and PTEN by ~50% at 1 and 10 μM, respectively (*SI Appendix*, Fig. S11). As miR-21 inhibition affects the invasive and metastatic properties of MDA-MB-231 cells, invasion assays were used to evaluate phenotype modulation. Treatment with **2** inhibited the invasive properties of MDA-

MB-231 (*SI Appendix*, Fig. S12). The biological effect of **2** was also studied in several other cancer cell model types (10–13) and in all cases **2** silenced miR-21 and modulated a miR-21–associated invasive phenotype (*SI Appendix*, Figs. S3 and S12).

To improve the potency of **2**, it was conjugated to a heterocyclic module that recruits latent ribonuclease (RNase L) to induce enzymatic cleavage of pre–miR-21 (14). Naturally, 2′-5′-linked oligoadenylates [2′-5′ poly(A)] dimerize and activate RNase L (15). A heterocyclic small molecule was previously identified to be a substitute for 2′-5′ poly(A) to modestly activate this process (16). Extensive optimization of this structure resulted in module **3** that can bind to inactive monomeric RNase L and dimerize it into an active nuclease; it is also suitable for conjugation to **2** to affect programmable cleavage (**5**; Figs. 2 and 3*A* and *SI Appendix*, Figs. S13 and S14). That is, **5** is a ribonuclease targeting chimera, or RIBOTAC. Additionally, an inactive RNase L recruiting compound (**4**) was identified with modest chemical changes to **3** (Fig. 2). Control compound **6**, which is the active RNase L recruiter without the miR-21–binding modules in **2**, and compound **7**, which is **2** appended to inactive recruiter **4**, were also synthesized and studied (Fig. 2).

Application of **5** to MDA-MB-231 cells showed 20-fold enhanced activity (IC_{50} ~ 0.05 μM) for reducing miR-21 levels over parent **2** (Fig. 3*B*). Control compound **7** did not have enhanced activity over **2**, while **6** was inactive (Fig. 3 *B* and *C*). Levels of pre–miR-21 were diminished with **5** as expected for a cleaving compound. Additional studies with **5** showed that it substoichiometrically cleaved pre–miR-21 in MDA-MB-231 cells as 1 mole of **5** cleaves 26 moles of pre–miR-21 (*SI Appendix*, Table S1), consistent with the enhancement in potency of **5** versus **2**. To further support that **5** directly cleaves pre–miR-21 via RNase L recruitment, it was demonstrated that: 1) siRNA ablation of RNase L decreased the ability of **5** to cleave pre–miR-21 (Fig. 3*C*); 2) addition of increasing amounts of **2** to cells with constant amounts of **5** competed away cleavage of pre–miR-21 as both bind to the same sites in pre–miR-21 (Fig. 3*D*); and 3) coimmunoprecipitation of RNase L from cells treated with **5** yielded increased levels of pre–miR-21 in the immunoprecipitated fraction (Fig. 3*E*).

To compare the potency of **2** and **5** and the duration of their effects, a time course for the reduction of mature miR-21 levels was completed (1.5–96 h posttreatment; *SI Appendix*, Fig. S15). Interestingly, reduction of mature miR-21 levels by **5** (50 nM) was statistically significant beginning at 12 h and this reduction was sustained until 96 h posttreatment. In contrast, a statistically significant effect by **2** (1,000 nM) was not observed until 24 h, with a similar reduction in mature miR-21 levels until 48 h. Its effect was then diminished at 72 h and completely lost by 96 h. These data indicate that compound **5** is more potent and has a more prolonged effect, as compared to **2**.

To assess the difference between enzymatic cleavage mediated by RNase L and nonenzymatic cleavage mediated by bleomycin, the effect of **5** and a bleomycin conjugate of **2** were tested in MDA-MB-231 cells. Enzymatic cleavage was 10-fold more potent (*SI Appendix*, Fig. S15). In addition, cleavage by **5** significantly inhibited miR-21 levels in various cancer cell lines, suggesting its broad applicability (*SI Appendix*, Fig. S15). To test whether nuclease recruitment can be generally applicable, a compound was designed to recruit RNase L to cleave pre–miR-210. Indeed, targeted cleavage of pre–miR-210 was observed, as expected (*SI Appendix*, Fig. S16).

During a viral infection, RNase L is dimerized and activated by 2′-5′poly(A). We therefore investigated whether **5** triggered antiviral and/or innate immune responses (17) as a first assessment of selectivity. As expected, up-regulation of the innate immune response was observed upon transfection of 2′-5′A₄ (500 nM), as evidenced by increased levels of mRNAs encoding innate immunity biomarkers (Ifng, OAS1, RIG-I, MDA5; measured by RT-qPCR) and increased IFN-γ protein levels (measured by enzyme-linked immunosorbent assay [ELISA]) (*SI Appendix*, Fig. S17). In
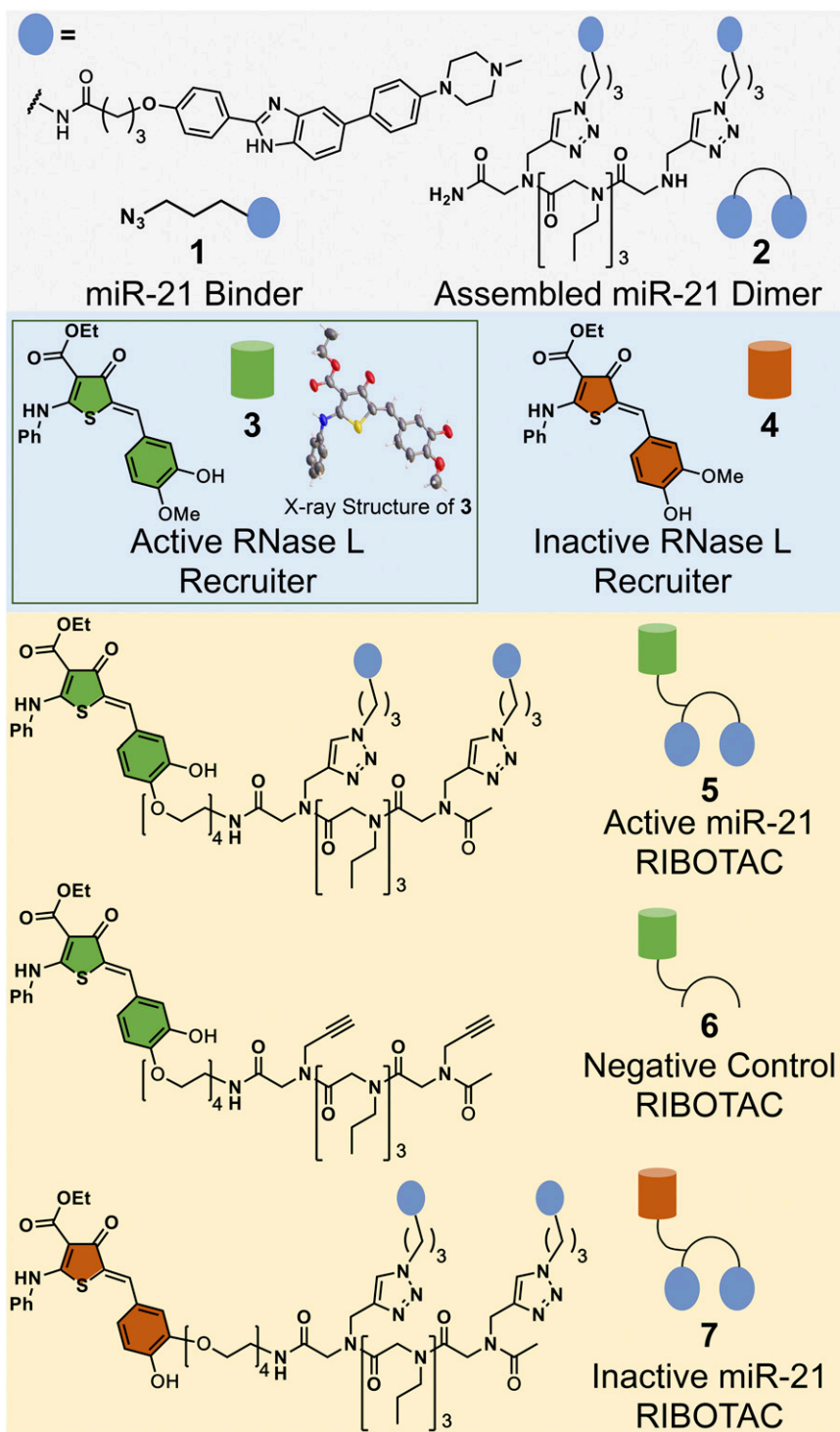
Fig. 2. Chemical structures of compounds used in this study. (*Top*, gray) Compounds that bind pre–miR-21 at the Dicer site to inhibit processing. (*Middle*, blue) Active (green) and inactive (orange) RNase L nuclease recruitment modules; an X-ray structure for compound **3** was solved and is shown in the ball and stick model (24). (*Bottom*, yellow) Active, inactive, and negative control compounds used in RNase L recruitment studies to enzymatically cleave pre–miR-21.

contrast, our compound that selectively recruits RNase L to pre–miR-21, **5**, did not up-regulate innate immunity markers at the mRNA or protein levels (*SI Appendix*, Fig. S17). Furthermore, pathway analysis of significantly changed proteins using Ingenuity Pathway Analysis and Search Tool for Retrieval of Interacting Genes/Proteins, which encompasses functional enrichments from classification systems such as Gene Ontology Resource Analysis

and the Kyoto Encyclopedia of Genes and Genomes pathways, showed no indication of up-regulated viral response pathways (*SI Appendix*, Tables S2 and S3). Collectively, these data suggest that compound **5** functions to locally activate RNase L, rather than globally initiate an antiviral innate immune response.

To quantify the effect of multivalency and nuclease recruitment on selectivity, we used cellular miR-inhibition profiles to
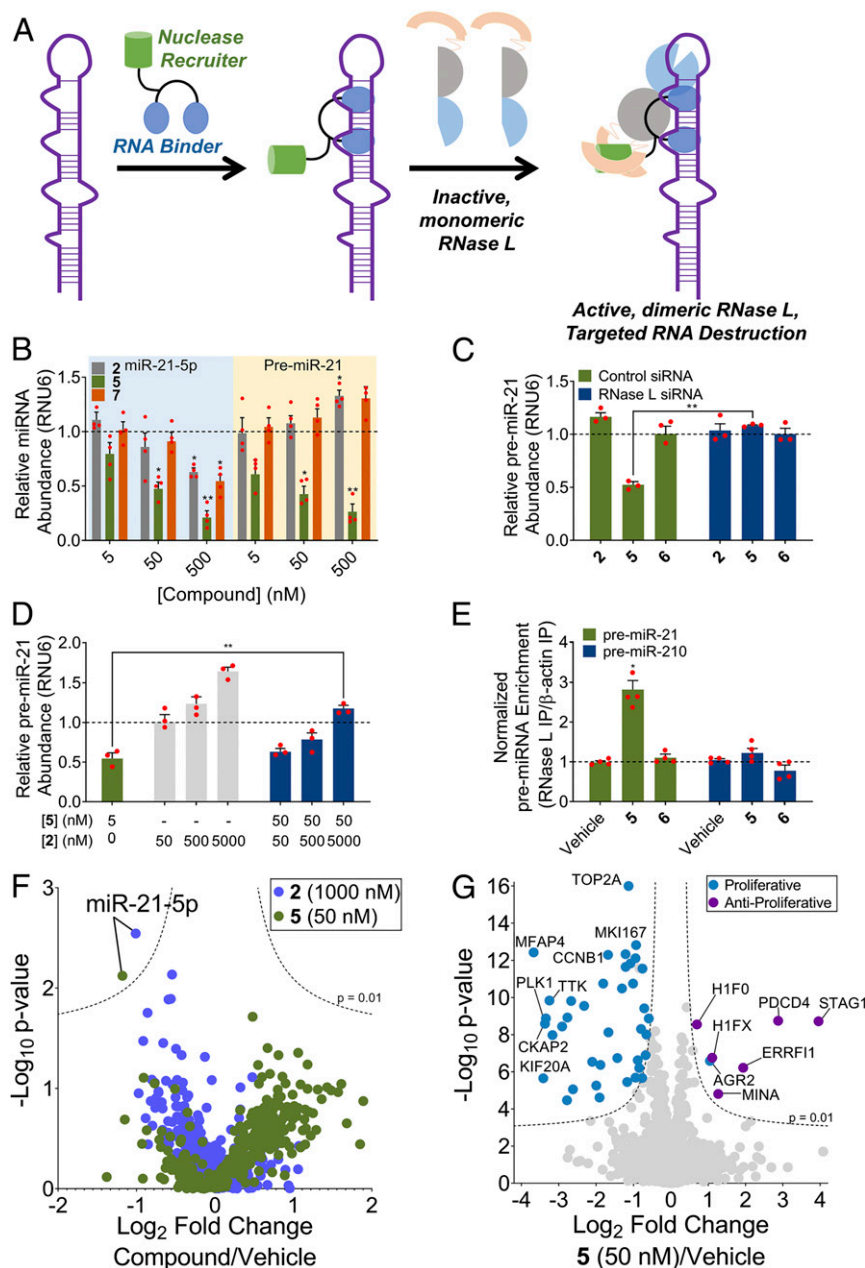
Fig. 3. Selective cleavage of pre–miR-21 by a small-molecule recruiter of RNase L in MDA-MB-231 cells. (*A*) Compound **5** dimerizes RNase L onto pre–miR-21 to enzymatically cleave it. (*B*) Compounds **2**, **5**, and **7** decreased miR-21 levels in MDA-MB-231. RNase L recruiting **5** decreased pre–miR-21 while **2** and **7** increased pre–miR-21 levels. (*C*) Diminished effects of **5** (50 nM) on pre–miR-21 were observed upon siRNA ablation of RNase L. (*D*) Cotreatment of **2** with **5** increased pre–miR-21 levels. (*E*) Coimmunoprecipitation of RNase L showed a ~3-fold increase in pre–miR-21 only with **5** (200 nM), while showing no enrichment of pre–miR-210. Data represent mean ± SEM ($n \geq 3$). *$P < 0.05$; **$P < 0.01$ as determined by a two-tailed Student t test. (*F*) RT-qPCR profiling of miRNAs in MDA-MB-231 with **2** (1,000 nM) and **5** (50 nM) treatment exhibited high selectivity for miR-21. (*G*) The majority of down-regulated proteins with **5**-treatment were proliferative proteins, while the majority of up-regulated proteins are anti-proliferative, as measured by global proteomics and pathway analysis. Dotted lines represent a false discovery rate of 1% and a group variance of $S_0(0.1)$.

calculate Gini Coefficients (GCs) for **1**, **2**, and **5**. A GC allows for selectivity to be scored in a single value; a GC of 0 indicates a nonselective compound while perfect selectivity has a GC of 1.0 (18). For reference, GCs of protein kinase inhibitors with high selectivity (e.g., inhibits 1/85 kinases tested) have scores ranging from 0.65 to 0.91. Compounds **1** and **2** have GCs of 0.52 and 0.68, respectively, demonstrating good selectivity (*SI Appendix,* Fig. S6). Importantly, an increase in selectivity was observed with nuclease recruiter **5** (GC = 0.84) (Fig. 3*F* and *SI Appendix,* Fig. S6). Furthermore, **5** showed no significant effects on a panel of

highly abundant transcripts that include ribosomal (r)RNAs, small (s)RNAs, transfer (t)RNAs, and messenger (m)RNAs, further demonstrating its broad selectivity (*SI Appendix,* Fig. S18) (19). Thus, nuclease recruitment does not diminish, but rather enhances potency and selectivity when compared to binders, and compounds designed to target RNA can be as selective as those that target proteins.

Since miR-21 stimulates an invasive phenotype in MDA-MB-231, the effect of **5** on invasion was measured. Indeed, **5** effectively inhibited invasion (*SI Appendix,* Fig. S19). Transient overexpression

of pre–miR-21 ablated the inhibitory effect of **5**, indicating it was due to targeting pre–miR-21. Additionally, **5** also decreased invasiveness broadly in melanoma and lung-cancer cell lines that express miR-21 (*SI Appendix*, Fig. S19). In contrast, **5** had no effect on invasion in MCF-10a, a model of healthy breast epithelial cells that does not appreciably express pre–miR-21. Transient transfection of pre–miR-21 into MCF-10a made the cell line invasive and application of **5** to MCF-10a under these conditions inhibited invasion (*SI Appendix*, Fig. S19).

The effect of **5** on the proteome of MBA-MB-231 cells was studied. Only 47 proteins of 4,181 were significantly affected (Dataset S1). The two most enhanced proteins were PDCD4, a direct target of miR-21, and STAG1, Cohesin subunit SA-1, which are involved in decreasing cellular proliferation and in protecting genome integrity, respectively (Fig. 3G and *SI Appendix*, Fig. S20 and Table S2). Pathway analysis of significantly modulated proteins found that **5** affected pathways involved in cell division and proliferation and regulation of the cell cycle (*SI Appendix*, Tables S2 and S3). Generally, proteins involved in genome stability were up-regulated while oncogenes were down-regulated. Importantly, the median log fold change of predicted downstream protein targets of miR-21 (TargetScanHuman v7.2) (20) following treatment by **5** was significantly up-regulated relative to all proteins (*SI Appendix*, Fig. S21). In contrast, no significant shift was observed among the downstream protein targets of similarly expressed miR-let-7–5p (*SI Appendix*, Fig. S21). Thus, effects on the proteome are selective and consistent with that expected upon miR-21 depletion.

To assess the ability of **5** to inhibit metastasis in vivo, we first measured its concentration in plasma of C57BL/6 mice post-intraperitoneal (i.p.) injection (10 mg/kg, quaque altera die [q.o.d.; every other day]) as a function of time. The compound was well tolerated, and low nanomolar concentrations were maintained in plasma up to 24 h postdelivery (*SI Appendix*, Fig. S22). Intravenous (i.v.) delivery of MDA-MB-231 cells to mice is a model of breast cancer metastasis, and metastatic behavior can be affected by inhibition of miR-21 (21). Compound treatment inhibited breast cancer metastasis to lung as evidenced by decreased lung nodules (Fig. 4A and *SI Appendix*, Fig. S23). Lung histological studies showed that **5** decreased hematoxylin and eosin (H&E) staining (Fig. 4B). To further validate **5**'s mode of action, we assayed mature and pre–miR-21 levels by RNA fluorescence in situ hybridization (FISH). As expected, miR-21 and pre–miR-21 levels were diminished, with no staining observed with the scrambled control FISH probe (Fig. 4 C and D and *SI Appendix*, Fig. S22). Immunohistochemistry showed that **5** stimulated an increase in PDCD4 protein expression (Fig. 4E). Thus, in a preclinical animal model **5** modulates a miR-21–mediated pathway.

Given the role of RNA structure in various disease settings, our RIBOTAC approach could be broadly applicable to deliver lead medicines and chemical probes targeting structured RNAs. The number of targets to which this approach can be applied will likely increase as more information on the RNA folds that are targets of small molecules emerges.

Methods

General Methods. General experimental procedures are given in *SI Appendix*.

Compound Synthesis. Details on synthesis and characterization of compounds are provided in *SI Appendix*.

Cell Culture. All cell lines were maintained as monolayers as previously described (14). Where indicated, cells cultured under hypoxic conditions were grown at 37 °C, 5% CO_2, and <1% O_2 in a nitrogen-filled hypoxic chamber (Billups-Rothenberg, Inc.). Growth medium for each cell line is as follows: MDA-MB-231 (American Type Culture Collection [ATCC]: HTB-26), Hepes-buffered Roswell Park Memorial Institute (RPMI) 1640 containing L-glutamine, 1× Antibiotic/Antimycotic solution (Corning), 1× Glutagro
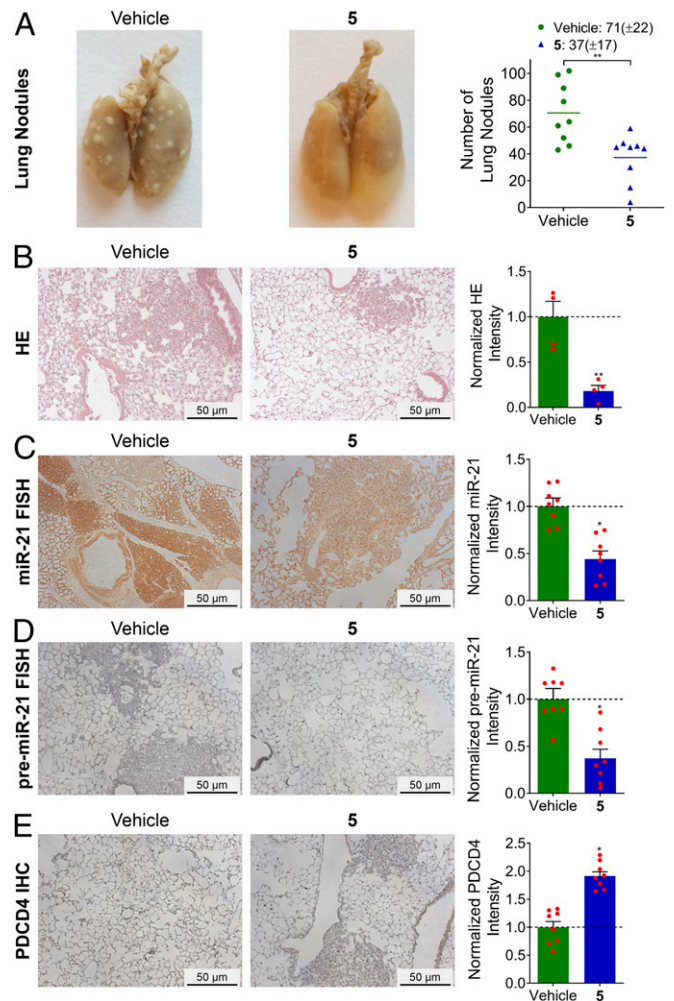

Fig. 4. Compound **5** inhibits metastasis of TNBC in vivo. (*A*) In vivo treatment of **5** (10 mg/kg, q.o.d., 6 wk) decreased lung nodules (white nodules) stained with Bouin's solution. (*B*) H&E staining of lung tissue from mice treated with **5** or vehicle. (*C*) Lung nodule tissue treated with **5**, but not vehicle, exhibited decreased mature miR-21 and (*D*) pre–miR-21 expression, as measured by FISH probing. (*E*) Treatment with **5** increased PDCD4 levels in lung nodule tissue sections as determined by immunohistochemistry (IHC) staining. (Scale bar, 50 µm.) Data represent mean ± SEM ($n \geq 4$). *$P < 0.05$; **$P < 0.01$ as determined by a two-tailed Student t test.

(Corning), and 10% fetal bovine serum (FBS) (Sigma); MDA-LM2, MDA-MB-231-Luc, HEK293T, A549 (ATCC: CCL-185), A375 (ATCC: CRL-1619), and MIA-PaCa-2 (ATCC: CRL-1420), 1× Dulbecco's modified eagle medium (DMEM) (high glycose), 1× Antibiotic/Antimycotic solution, 1× Glutagro, and 10% FBS; MCF-10a (ATCC: CRL-10317), 1× Hepes-buffered DMEM/F-12 containing L-glutamine (Corning), human insulin (10 µg/mL; Sigma-Aldrich), hydrocortisone (0.5 mg/mL; Pfaltz & Bauer) and human epidermal growth factor (20 ng/mL; Pepro Tech), 1× Antibiotic/Antimycotic solution, and 10% FBS.

RNA Isolation and RT-qPCR. Total RNA was extracted from cells by using a Quick-RNA MiniPrep (Zymo Research) according to the manufacturer's protocol. Approximately 100–1,000 ng of total RNA was used in subsequent reverse transcription reactions. For miRs, reverse transcription was completed using a miScript II RT Kit (Qiagen) while a qScript cDNA Synthesis Kit (QuantaBio) was used for all other RNA types, both completed per the manufacturer's recommended protocol. The sequences of RT-qPCR primers (purchased from Eurofins or Integrated DNA Technologies, Inc.) are provided in *SI Appendix*, Table S4. After RT, qPCR was completed using Power SYBR Green PCR Master Mix (Applied Biosystems) and a 7900HT Fast Real Time PCR System (Applied Biosystems). RNA levels were calculated using the ΔΔCt method and normalized to 18S, GAPDH, or U6 small nuclear RNA.

RNA Immunoprecipitation. Immunoprecipitation studies were completed as previously described (22), with the following modifications: 1) MDA-MB-231 cells (~70% confluency in 6-well plates) were treated with 200 nM of 2′-5′ A_4 or 200 nM **5** (200 nM), prepared in growth medium, for 48 h; 2) cells were lysed in 100 μL of M-PER Buffer supplemented with 80 U RNaseOUT Recombinant Ribonuclease Inhibitor (Invitrogen) and 1× Protease Inhibitor Mixture III for Mammalian Cells (Research Products International Corp.) according to the manufacturer's recommendations. Normalized fold change was calculated using Eq. 1 (22):

$$\text{Normalized Fold Change} = \frac{\text{Relative RNA Expression in RNase L fraction}}{\text{Relative RNA Expression in } \beta\text{-actin fraction}}.$$

[1]

Lung Nodule Metastasis Study. Female nonobese diabetic/severe combined immunodeficiency (NOD/SCID) mice (n = 8, 5–7 wk) were used for in vivo studies. Mice were purchased from Jackson Laboratory and were housed in the Scripps Florida vivarium. All experiments using live animals were approved by the Scripps Florida Institutional Animal Care and Use Committee. The MDA-MB-231 cells stably transfected with luciferase (MDA-MB-231-Luc) were harvested by trypsinization, washed twice in phosphate-buffered saline (PBS), and counted. A total of 0.8×10^6 cells was i.v. injected into NOD/SCID mice tail veins. Mice were imaged for luciferase activity immediately after injection to exclude any animal that was not successfully xenografted. After cell implantation, the luciferase signal was monitored after injection of cells every other day to determine initial compound treatment. Mice were anesthetized and injected intraperitoneally with 100 μL of D-luciferin solution (30 mg/mL in PBS). Imaging was performed with 90-s exposure time using a Lago X In Vivo Imager (Spectral Instruments).

After 3 d, the mice were split into two groups with the same mean luciferase signal. The vehicle group was dosed with DMSO/Tween-80/H_2O (10/10/80) and the compound treatment group was dosed with 10 mg/kg **5** in DMSO/Tween-80/H_2O (10/10/80). Dosing was performed every other day, and the weight of each mouse was monitored. Luciferase activity was monitored every week. After 6 wk of dosing, the mice were euthanized (in accordance with guidelines provided by the American Veterinarian Medical Association), the lungs were perfused with PBS and harvested. The harvested lungs were fixed in Bouin's solution (Sigma: HT10132-1L) immediately for less than 24 h. The lung nodule metastases were then counted, and then the fixed lung

tissues were immersed into 50 mL of 10% formalin solution and washed eight times over 48 h to remove the Bouin's solution. Lungs were then given to the Histology Core at Scripps Research Florida to prepare paraffin-embedded sections for the next staining steps.

Lung Tissue Histology for H&E Staining, miR-21 Staining, and PDCD4 Staining. The tissue samples were processed and embedded in paraffin and sectioned at 3 μm. To assess levels of PDCD4, an anti-PDCD4 (rb) antibody (Abcam; ab51495) was used, diluted to a final concentration of 1:100. The slides were stained with a Leica Bond-Max immunostaining platform using a DAB Refine kit. Negative control slides were stained by the same protocol but without applying the primary antibody. After staining, slides were dehydrated in graded alcohols, cleared in xylenes, and coverslipped with Cytoseal 60. All histology staining (H&E and PDCD4) was performed by the Histology Core at Scripps Florida.

Pre- and mature miR-21 were imaged by RNA FISH, as previously described (23), with the following modifications: 1) the prepared paraffin-embedded sections were first incubated at 60 °C overnight, followed by deparaffinization through three consecutive xylene baths (5 min each); 2) custom-synthesized oligonucleotides (0.2 μM) with locked nucleic acid modifications and 3′ end labeling with fluorescein isothiocyanate (FITC) (Qiagen) were used to probe for miR-21, pre–miR-21, or a scrambled control sequence were incubated with the tissue sections at 37 °C overnight; and 3) post-hybridization, slides were washed three times with 2× saline-sodium citrate (SSC) at room temperature for 15 min each, followed by three washes with PBS for 15 min each.

Where indicated, slides were stained with Mayer's Hematoxylin Solution (Sigma: MHS1-100ML) per the manufacturer's protocol.

Images of all slides were obtained using light microscopy on a Leica DMI3000 B upright fluorescent microscope.

1. X. Wu, D. P. Bartel, Widespread influence of 3′-end structures on mammalian mRNA processing and stability. *Cell* **169**, 905–917.e11 (2017).
2. L. Sun *et al.*, RNA structure maps across mammalian cellular compartments. *Nat. Struct. Mol. Biol.* **26**, 322–330 (2019).
3. D. P. Bartel, MicroRNAs: Genomics, biogenesis, mechanism, and function. *Cell* **116**, 281–297 (2004).
4. A. M. Krichevsky, G. Gabriely, miR-21: A small multi-faceted RNA. *J. Cell Mol. Med.* **13**, 39–53 (2009).
5. S. P. Velagapudi, S. M. Gallo, M. D. Disney, Sequence-based design of bioactive small molecules that target precursor microRNAs. *Nat. Chem. Biol.* **10**, 291–297 (2014).
6. Z. Su *et al.*, Discovery of a biomarker and lead small molecules to target r(GGGGCC)-associated defects in c9FTD/ALS. *Neuron* **84**, 239 (2014).
7. D. Iliopoulos, S. A. Jaeger, H. A. Hirsch, M. L. Bulyk, K. Struhl, STAT3 activation of miR-21 and miR-181b-1 via PTEN and CYLD are part of the epigenetic switch linking inflammation to cancer. *Mol. Cell* **39**, 493–506 (2010).
8. L. B. Frankel *et al.*, Programmed cell death 4 (PDCD4) is an important functional target of the microRNA miR-21 in breast cancer cells. *J. Biol. Chem.* **283**, 1026–1033 (2008).
9. N. M. McLoughlin, C. Mueller, T. N. Grossmann, The therapeutic potential of PTEN modulation: Targeting strategies from gene to protein. *Cell Chem. Biol.* **25**, 19–29 (2018).
10. M. J. Hendrix *et al.*, Retinoic acid inhibition of human melanoma cell invasion through a reconstituted basement membrane and its relation to decreases in the expression of proteolytic enzymes and motility factor receptor. *Cancer Res.* **50**, 4121–4130 (1990).
11. M. Seike *et al.*, MiR-21 is an EGFR-regulated anti-apoptotic factor in lung cancer in never-smokers. *Proc. Natl. Acad. Sci. U.S.A.* **106**, 12085–12090 (2009).
12. S. F. Tavazoie *et al.*, Endogenous human microRNAs that suppress breast cancer metastasis. *Nature* **451**, 147–152 (2008).
13. F. Sicard, M. Gayral, H. Lulka, L. Buscail, P. Cordelier, Targeting miR-21 for the therapy of pancreatic cancer. *Mol. Ther.* **21**, 986–994 (2013).
14. M. G. Costales, Y. Matsumoto, S. P. Velagapudi, M. D. Disney, Small molecule targeted recruitment of a nuclease to RNA. *J. Am. Chem. Soc.* **140**, 6741–6744 (2018).
15. Y. Han *et al.*, Structure of human RNase L reveals the basis for regulated RNA decay in the IFN response. *Science* **343**, 1244–1248 (2014).
16. C. S. Thakur *et al.*, Small-molecule activators of RNase L with broad-spectrum antiviral activity. *Proc. Natl. Acad. Sci. U.S.A.* **104**, 9585–9590 (2007).
17. A. Chakrabarti, B. K. Jha, R. H. Silverman, New insights into the role of RNase L in innate immunity. *J. Interferon Cytokine Res.* **31**, 49–57 (2011).
18. P. P. Graczyk, Gini coefficient: A new way to express selectivity of kinase inhibitors against a family of kinases. *J. Med. Chem.* **50**, 5773–5779 (2007).
19. W. Y. Yang, R. Gao, M. Southern, P. S. Sarkar, M. D. Disney, Design of a bioactive small molecule that targets r(AUUCU) repeats in spinocerebellar ataxia 10. *Nat. Commun.* **7**, 11647 (2016).
20. V. Agarwal, G. W. Bell, J.-W. Nam, D. P. Bartel, Predicting effective microRNA target sites in mammalian mRNAs. *eLife* **4**, e05005 (2015).
21. S. Yang, J. J. Zhang, X.-Y. Huang, Mouse models for tumor metastasis. *Methods Mol. Biol.* **928**, 221–228 (2012).
22. M. G. Costales, B. Suresh, K. Vishnu, M. D. Disney, Targeted degradation of a hypoxia-associated non-coding RNA enhances the selectivity of a small molecule interacting with RNA. *Cell Chem. Biol.* **26**, 1180–1186.e5 (2019).
23. N. Yamamichi *et al.*, Locked nucleic acid in situ hybridization analysis of miR-21 expression during colorectal cancer development. *Clin. Cancer Res.* **15**, 4009–4016 (2009).
24. P. HaJeung *et al.*, ethyl (Z)-5-(3-hydroxy-4-methoxybenzylidene)-4-oxo-2-(phenyl-amino)-4,5-dihydrothiophene-3-carboxylate. The Cambridge Crystallographic Data Centre (CCDC). https://www.ccdc.cam.ac.uk/structures/Search?Ccdcid=1912054&DatabaseToSearch=Published. Deposited 24 April 2019.